

Neural Galerkin Scheme with Active Learning for High-Dimensional Evolution Equations

Joan Bruna* Benjamin Peherstorfer* Eric Vanden-Eijnden*

March 4, 2022

Machine learning methods have been shown to give accurate predictions in high dimensions provided that sufficient training data are available. Yet, many interesting questions in science and engineering involve situations where initially no data are available and the principal aim is to gather insights from a known model. Here we consider this problem in the context of systems whose evolution can be described by partial differential equations (PDEs). We use deep learning to solve these equations by generating data on-the-fly when and where they are needed, without prior information about the solution. The proposed Neural Galerkin schemes derive nonlinear dynamical equations for the network weights by minimization of the residual of the time derivative of the solution, and solve these equations using standard integrators for initial value problems. The sequential learning of the weights over time allows for adaptive collection of new input data for residual estimation. This step uses importance sampling informed by the current state of the solution, in contrast with other machine learning methods for PDEs that optimize the network parameters globally in time. This active form of data acquisition is essential to enable the approximation power of the neural networks and to break the curse of dimensionality faced by non-adaptative learning strategies. The applicability of the method is illustrated on several numerical examples involving high-dimensional PDEs, including advection equations with many variables, as well as Fokker-Planck equations for systems with several interacting particles.

Keywords: partial differential equations | high dimensions | deep networks | adaptive data acquisition | importance sampling

1. Introduction

Partial differential equations (PDEs) are used to describe the dynamics of systems in a wide variety of science and engineering applications. Unfortunately few of these equations can be solved, either analytically or even numerically. Classical techniques from scientific computing such as the finite element method and other grid-based methods can work well if the solution domain is low dimensional; however, in higher dimensions, grid-based methods fail because their computational costs increase at an exponential rate with the dimension of the domain. This curse of dimensionality leaves simulating many systems of interest out of scope of classical PDE solvers. For example, interacting particles described by Schrödinger's and other kinetic equations such as Fokker-Planck and Boltzmann equations lead to high-dimensional systems when the number of particles is more than a few. Even multiscale techniques as sophisticated as multigrid, fast multipole, and adaptive-mesh refinement methods fail in such instances. In essence, high-dimensional approximation problems require a fundamentally different notion of "off-the-grid" adaptivity to circumvent the curse of dimensionality. In

*Courant Institute of Mathematical Sciences, New York University, New York, NY 10012

supervised machine learning applications, such adaptivity is achieved with deep neural networks (DNNs) via feature or *representation* learning.

The last few years have seen many developments in the direction of using DNNs for numerically solving PDEs, with the introduction of techniques such as physics-informed neural networks and the Deep Ritz method [4, 21, 17, 2]. In these schemes, the solution of a time-dependent PDE is represented with a DNN and the parameters of the network are optimized by minimizing the residual of the PDE on collocation points from the temporal and spatial domains. These collocation points can lie on a grid, or be sampled randomly in time-space. Either way, their positions are usually not tailored to the (unknown) solution of the PDE. In high dimension, such lack of adaptivity in the training procedure ultimately suffers from the curse of dimensionality because all features of the solution have to be discovered without guidance. In addition, the training treats space and time in a symmetrical way, which is inefficient for initial value problems if we want to predict the PDE solution over long times.

In this work we take a different approach. We develop time-integrators for PDEs that use DNNs to represent the solution but update the parameters sequentially from one time slice to another rather than globally over the whole time-space domain, as was also proposed in [6], thereby allowing for collecting data on the way and for integration over arbitrary long time intervals. The scheme uses the structural form of the PDEs, but no *a priori* data about their solution. Since in practice the neural network approximation introduces errors, the scheme is designed to minimize the PDE residual as the solution is evolved in time. Evaluating this residual in turn requires either a quadrature rule or generating samples to produce a faithful estimator—the analog of the training data in supervised learning. While on low-dimensional problems either strategy can be carried out efficiently, the situation in higher dimensions introduces an additional challenge, namely how to efficiently estimate (and ultimately minimize) the residual errors. For that purpose, we introduce an adaptive sampling scheme that addresses the non-stationary and intermittent nature of these errors. In other words, we leverage adaptivity in *both* function approximation and data acquisition.

Main contributions: 1. Given a nonlinear parametric representation (e.g. via a DNN) of the solution of an initial value problem for a time-dependent PDE, we show how to derive a nonlinear evolution equation for the parameters in this representation. This equation can then be integrated using standard solvers with different level of sophistication, for example by dynamically choosing the time-step size based on properties of the numerical solution. In particular, with suitable time-integration schemes, the proposed approach takes larger time steps when possible and corrects to smaller time-step sizes if the dynamics of the solution require it. This is in contrast to typical collocation methods such as the Deep Ritz Method that samples over the whole time-space domain without having the opportunity to exploit the smoothness of solutions over time and thus have to draw samples even when the solution hardly varies.

2. The evolution equations that we derive for the DNN parameters involve operators that require estimation via sampling in space. We show how to perform this sampling adaptatively, by using the property of the current solution itself, which is again in contrast to collocation methods. We propose a dynamical estimation of the loss, which is shown to be essential in two aspects: First it achieves accuracy in situations where static, non-adaptive sampling methods fail to capture the details of the solution that determine its evolution. Second, it is key to the interpretation of the PDE solution itself, since this solution can be quite complicated, and sampling its feature typically is the only way to exploit and interpret it.

3. We illustrate the viability and usefulness of our approach on a series of test cases. First we consider two equations in low dimensions, the Korteweg-de Vries (KdV) and the Allen-Cahn (AC) equations to show that our method can be used to efficiently capture solutions with localized features that move in the spatial domain. The features are solitons in the context of the KdV equation and domain walls in the context of the AC equation, which can both be modeled with few degrees of freedom using neural networks with specific nonlinear units. Second, we show that our method can be used to simulate PDEs in unbounded, high-dimensional domains, that are out of reach of standard methods. Specifically, we study advection equations of hyperbolic type with wave speeds that vary in space and time, and Fokker-Planck equations of parabolic type for the evolution of several interacting particles. In both cases, our results show that our

method is able to efficiently capture the evolution of the solution and overcome the sampling limitations of collocation-based methods.

Related works: The need for adaptive data acquisition in the context of machine learning for problems in science and engineering has been emphasized in previous works [19]. There also is a large body of work on numerically solving PDEs with DNN parametrization based on collocation over the spatiotemporal domain (space-time discretizations), which makes adaptive sampling challenging; see, e.g., Refs. [4, 21, 17, 2]. Methods that do not rely on collocation typically exploit specific formulations of elliptic and semilinear parabolic PDEs [7, 10], and focus on specific approximation tasks such as learning committor functions [11, 19], coarse-graining [1, 13, 24], or de-noising [20]. Thus, these approaches are limited in their scope and, in particular, are not applicable to pure transport dynamics given by kinetic and hyperbolic equations. There also is a range of surrogate-modeling methods based on nonlinear parametrizations such as [23, 14, 3, 12, 15]; however, these methods require access to training sets of ground truth PDE solutions, which is precisely what is unavailable in our setting because classical PDE solvers are cursed by dimension. The surrogate-modeling method introduced in [15] embeds large state vectors stemming from traditional discretizations of PDEs in low-dimensional manifolds and then propagates forward in time the embedding based on the dynamics given by the traditional discretizations; however, this means that in each time step a lifting from low to high dimensions has to be performed, which is inherently computationally expensive. In contrast, the proposed Neural Galerkin scheme directly integrates the parameters of the PDE solutions, rather than embeddings of high-dimensional states. This approach circumvents the requirement of needing traditional discretizations of the underlying PDEs, which avoids the expensive lifting to higher dimensions that is intractable for problems formulated over high-dimensional spatial domains.

Closest to our model is the work in [6], which also proposes to integrate the DNN parametrizations of PDE solutions sequentially in time. However, Ref. [6] focuses exclusively on low-dimensional problems where data acquisition with static, uniform sampling is tractable. In contrast, our Neural Galerkin scheme with adaptive sampling applies to high-dimensional problems where adaptive data collection becomes crucial, as illustrated by our case studies.

2. Neural Galerkin schemes

2.1. Neural Galerkin

Given a spatial domain $\mathcal{X} \subseteq \mathbb{R}^d$, we will consider the evolution of a time-dependent field $u : [0, \infty) \times \mathcal{X} \rightarrow \mathbb{R}$ which at all times belongs to some function space \mathcal{U} and whose dynamics is governed by

$$\begin{cases} \partial_t u(t, \mathbf{x}) = f(t, \mathbf{x}, u) & \text{for } (t, \mathbf{x}) \in [0, \infty) \times \mathcal{X} \\ u(0, \mathbf{x}) = u_0(\mathbf{x}) & \text{for } \mathbf{x} \in \mathcal{X} \end{cases} \quad (1)$$

where $u_0 \in \mathcal{U}$ is the initial condition. By appropriately choosing $f : [0, \infty) \times \mathcal{X} \times \mathcal{U} \rightarrow \mathbb{R}$, Eq. (1) can represent different equations of interest: for example, we get an advection-diffusion-reaction equation by taking $f(t, \mathbf{x}, u) = b(t, \mathbf{x}) \cdot \nabla u + a(t, \mathbf{x}) : \nabla \nabla u + G(t, \mathbf{x}, u)$ for some $b : [0, \infty) \times \mathcal{X} \rightarrow \mathbb{R}^d$, $a : [0, \infty) \times \mathcal{X} \rightarrow \mathbb{R}^d \times \mathbb{R}^d$, and $G : [0, \infty) \times \mathcal{X} \times \mathbb{R} \rightarrow \mathbb{R}$. We assume that there are appropriate boundary conditions for Eq. (1) that make Eq. (1) well-posed for all $t \in [0, \infty)$, i.e. that its solution exists, is unique, and depends continuously on $u_0 \in \mathcal{U}$.

Parametrizing the solution

To proceed we parametrically represent the solution $u(t)$ at time t as $U(\theta(t)) \in \mathcal{U}$ with parameters $\theta(t) \in \Theta$ and $U : \Theta \times \mathcal{X} \rightarrow \mathbb{R}$, i.e. we use the ansatz

$$u(t, \mathbf{x}) = U(\theta(t), \mathbf{x}) \quad \text{for } (t, \mathbf{x}) \in [0, \infty) \times \mathcal{X}. \quad (2)$$

It is important to emphasize that U may depend *nonlinearly* on $\theta(t)$, which is in stark contrast to the majority of classical approximations in scientific computing that have a linear dependence on the parameter; see, e.g., Ref. [8]. In order for the representation in Eq. (2) to be complete, i.e. such that for any $u(t) \in \mathcal{U}$ there exists at least one $\theta(t) \in \Theta$ such that $U(\theta(t)) \equiv u(t)$, Θ should itself be an infinite-dimensional function space in general—for more discussion on this point, see Section A in the Appendix. In practice, however, we will be interested in situations where the parametric representation U depends on a finite-dimensional parameter $\theta(t)$ such as in a DNN, where $\theta(t)$ denotes the vector of adjustable parameters/weights in this network whose number can be large but is finite—specific DNN representations are discussed below. In this case, using Eq. (2) as ansatz for the solution of Eq. (1) introduces approximation errors, the magnitude of which we aim to control at all times.

Controlling the residual

Since we do not have access to the solution $u(t)$, we will use the structure of the governing equation (1) to control the approximation error. To this end, note that inserting the ansatz solution $U(\theta(t))$ in Eq. (1), assuming differentiability of $\theta(t)$ and using $\partial_t U(\theta(t)) = \nabla_\theta U(\theta) \cdot \dot{\theta}(t)$, leads to the residual function $r : \Theta \times \dot{\Theta} \times \mathcal{X} \rightarrow \mathbb{R}$ defined as

$$r_t(\theta, \eta, \mathbf{x}) \equiv \nabla_\theta U(\theta, \mathbf{x}) \cdot \eta - f(t, \mathbf{x}, U(\theta)), \quad (3)$$

where $\dot{\Theta}$ is the set of time derivatives of $\theta(t)$. A natural way to control the error made by the parametrization described in Eq. (2) is to minimize the magnitude of the residual r_t with respect to η , given an appropriate metric. One possibility is to do so globally over some time interval $t \in [0, T]$ with $T > 0$; this option, which is discussed in Section C in the Appendix, has the disadvantage that it leads to a complicated boundary value problem that requires the storage of the entire path $\theta(t)$ for $t \in [0, T]$. Instead, similar to what was proposed in [6], we will opt for controlling the residual locally in time, which leads to an initial value problem that can be solved over arbitrary long times. Specifically, we will seek $\theta(t)$ such that for all $t > 0$ it holds

$$\dot{\theta}(t) \in \underset{\eta \in \dot{\Theta}}{\operatorname{argmin}} J_t(\theta(t), \eta) \quad (4)$$

where we define the objective function $J_t : \Theta \times \dot{\Theta} \rightarrow \mathbb{R}$ as

$$J_t(\theta, \eta) = \frac{1}{2} \int_{\mathcal{X}} |r_t(\theta, \eta, \mathbf{x})|^2 d\nu_\theta(\mathbf{x}). \quad (5)$$

The explicit form of Eq. (4) is the system of first-order ordinary differential equations (ODEs) given in Eq. (7) below; in Eq. (5), ν_θ is a positive measure with full support on \mathcal{X} that needs to be user-prescribed and may depend on the current state θ of the parameters. How to specify this measure will be discussed in detail below: it is a critical aspect of our method in terms of its accuracy and efficiency, since in practice we need to numerically estimate the objective J_t (or rather its derivative in η) from samples drawn in \mathcal{X} . This estimation is nontrivial when \mathcal{X} is high dimensional and will require us to exploit the features of the solution $U(\theta(t))$ in a time-adaptive way.

Neural Galerkin equations

Since $J_t(\theta(t), \eta)$ is quadratic in η and positive semi-definite, its minimum is unique and its minimizers solve the Euler-Lagrange equation

$$\nabla_\eta J_t(\theta(t), \dot{\theta}(t)) = 0. \quad (6)$$

Written explicitly, Eq. (6) is a system of ODEs for $\theta(t)$:

$$M(\theta)\dot{\theta} = F(t, \theta), \quad \theta(0) = \theta_0, \quad (7)$$

where we defined

$$\begin{aligned} M(\theta) &= \int_{\mathcal{X}} \nabla_{\theta} U(\theta, \mathbf{x}) \otimes \nabla_{\theta} U(\theta, \mathbf{x}) d\nu_{\theta}(\mathbf{x}) \\ F(t, \theta) &= \int_{\mathcal{X}} \nabla_{\theta} U(\theta, \mathbf{x}) f(t, \mathbf{x}, U(\theta)) d\nu_{\theta}(\mathbf{x}), \end{aligned} \tag{8}$$

in which \otimes denotes the outer product. The initial condition θ_0 can be obtained via e.g. minimization of the least-squares loss between u_0 and $U(\theta_0)$:

$$\theta_0 \in \operatorname{argmin}_{\theta \in \Theta} \int_{\mathcal{X}} |u_0(\mathbf{x}) - U(\theta, \mathbf{x})|^2 d\nu(\mathbf{x}) \tag{9}$$

where ν is some user-prescribed measure with full support on \mathcal{X} . Similarly, boundary conditions can be enforced either naturally by choosing $U(\theta(t))$ such that these conditions are satisfied for all $\theta(t) \in \Theta$, or by adding appropriate penalty terms to the residual (3) and the objective (5). For more justification of Eq. (7) note that this equation also arises as a consequence of Proposition 1 in the Appendix.

The dynamical equation (7) for $\theta(t)$ is the basis for the numerical schemes we introduce below. We refer to $U(\theta(t))$ as Neural Galerkin solution because Eq. (7) can be derived via testing the residual $r_t(\theta, \dot{\theta}, \mathbf{x})$ in Eq. (3) using $\nabla_{\theta} U(\theta, \mathbf{x})$ as test function and Galerkin projection with respect to the inner product of $L^2(\mathcal{X}; \nu_{\theta})$. The objective function (5) also arises if we take the inner product between $r_t(\theta, \dot{\theta}, \mathbf{x})$ and a test function $g(\mathbf{x})$ and maximize it over all $g(\mathbf{x})$ with norm one in $L^2(\mathcal{X}; \nu_{\theta})$.

Solving Eq. (7) numerically now requires dealing with three issues: (i) estimating the operators $M(\theta)$ and $F(t, \theta)$ defined in (8) after proper specification of the measure ν_{θ} ; (ii) designing a discrete time-integrator to solve (7) in time; and (iii) choosing the parametrization $U(\theta)$, i.e. the neural network architecture.

2.2. Estimating $M(\theta)$ and $F(t, \theta)$

For generic choices of parametrization $U(\theta)$, the integrals in Eq. (8) do not admit a closed-form solution and so will need to be numerically estimated. In low dimensions, this calculation can be performed by quadrature on a grid. When \mathcal{X} is high dimensional, however, this approach fails and we must proceed differently. If ν_{θ} is a probability measure, we can consider using a vanilla Monte-Carlo estimator for each term, by drawing n samples $\{\mathbf{x}_i\}_{i=1}^n$ from ν_{θ} and replacing the expectations by empirical averages over these samples. This estimator is efficient to approximate certain kernels uniformly over high-dimensional spaces [16], but not necessarily if the solution to the PDE (1) develops spatially localized structures, as is the case in many physical systems of interest. In these situations, the estimation of $M(\theta)$ and $F(t, \theta)$ must be informed by the solution itself, i.e. we must use some strategy adapted to $U(\theta)$ [19]. Here we give two options:

Importance sampling with a fixed measure

Suppose that we use a fixed measure $\nu_{\theta} = \nu$ in Eq. (8). We can then perform importance sampling on this measure by defining some positive weights $\omega : \mathcal{X} \times \Theta \rightarrow (0, \infty)$ such that $Z_{\theta} = \int_{\mathcal{X}} \omega(\mathbf{x}, \theta) d\nu(\mathbf{x}) < \infty$ for all $\theta \in \Theta$, drawing samples $\{\mathbf{x}_i\}_{i=1}^n$ from $d\nu_{\theta}(\mathbf{x}) = Z_{\theta}^{-1} \omega(\mathbf{x}, \theta) d\nu(\mathbf{x})$, and using the reweighted estimators \tilde{M} and \tilde{F} given by

$$\begin{aligned} \tilde{M}(\theta) &= \frac{1}{n} \sum_{i=1}^n \frac{\nabla_{\theta} U(\theta, \mathbf{x}_i) \otimes \nabla_{\theta} U(\theta, \mathbf{x}_i)}{\omega(\mathbf{x}_i, \theta)}, \\ \tilde{F}(t, \theta) &= \frac{1}{n} \sum_{i=1}^n \frac{\nabla_{\theta} U(\theta, \mathbf{x}_i) f(t, \mathbf{x}_i, U(\theta))}{\omega(\mathbf{x}_i, \theta)}. \end{aligned} \tag{10}$$

For these estimators to be effective, their variances must be relatively small, which requires choosing the weights $\omega(\mathbf{x}, \theta)$ in a way that is informed by the solution $U(\theta, \mathbf{x})$. This choice must be made on a case-by-case basis. For example, below we consider Fokker-Planck equations whose solutions are normalized

probability density functions: in this case, it is natural to take $d\nu(\mathbf{x}) = d\mathbf{x}$ and $\omega(\mathbf{x}, \theta) = U(\theta, \mathbf{x})$ so that $d\nu_\theta(\mathbf{x}) = U(\theta, \mathbf{x})d\mathbf{x}$ (since we must have $\int_{\mathcal{X}} U(\theta, \mathbf{x})d\mathbf{x} = 1$)—this choice will lead to low variance estimators if the density has mass localized in a few relatively small regions that move in \mathcal{X} . If in addition the parametrization $U(\theta)$ involves a Gaussian mixture, as in the Fokker-Planck examples below, sampling from it is straightforward—with this specific choice we can in fact evaluate analytically the integrals of the components of $M(\theta)$ and sampling is only required to estimate $F(t, \theta)$. Other choices for the weights are possible too, e.g. by taking $\omega(\mathbf{x}, \theta)$ proportional to $|\nabla_{\mathbf{x}}U(\theta, \mathbf{x})|$ in situations where the solution has localized fronts that propagate in \mathcal{X} .

Direct sampling with an adaptive measure

The second option is to simply take a probability measure ν_θ informed by the solution $U(\theta)$, specified e.g. as above, and use this measure directly in Eq. (8). With this choice, if $\{\mathbf{x}_i\}_{i=1}^n$ are again samples from ν_θ , we get estimators for $M(\theta)$ and $F(t, \theta)$ similar to the ones in Eq. (10), but without the weights:

$$\begin{aligned}\tilde{M}(\theta) &= \frac{1}{n} \sum_{i=1}^n \nabla_{\theta}U(\theta, \mathbf{x}_i) \otimes \nabla_{\theta}U(\theta, \mathbf{x}_i), \\ \tilde{F}(t, \theta) &= \frac{1}{n} \sum_{i=1}^n \nabla_{\theta}U(\theta, \mathbf{x}_i) f(t, \mathbf{x}_i, U(\theta)).\end{aligned}\tag{11}$$

In the high-dimensional examples presented below, we used this simpler strategy since Eq. (10) has no clear *a priori* advantage over Eq. (11).

2.3. Discretization in time

Eq. (7) are a set of ODEs that can be numerically integrated using standard methods. Let us denote by θ^k the numerical approximation to $\theta(t_k)$ where the times t_k with $k = 0, 1, 2, \dots$ are defined recursively via $t_0 = 0$, $t_{k+1} = t_k + \delta t_k$ using the time steps $\delta t_k > 0$, possibly nonuniform and chosen adaptively. To update θ^k , we can either use:

Explicit integrators

The forward Euler scheme is an explicit scheme that leads to (plugging the estimators defined in (10) or (11) for M and F into Eq. (7))

$$\tilde{M}(\theta^k)\theta^{k+1} = \tilde{M}(\theta^k)\theta^k - \delta t_k \tilde{F}(t_k, \theta^k).\tag{12}$$

This is an explicit equation for θ^{k+1} which is solved at every time step—to this end it may be useful to add a regularizing term λId to \tilde{M} . Other integrators can be used as well, such as the adaptive Runge–Kutta–Fehlberg (RK45) method [5], which leads to linear systems similar to (12) at every stage—RK45 will be used in the examples below.

Implicit integrators

We consider the backward Euler scheme as an example for implicit integrators, which leads to the system of equations

$$\tilde{M}(\theta^{k+1})\theta^{k+1} = \tilde{M}(\theta^{k+1})\theta^k - \delta t_k \tilde{F}(t_{k+1}, \theta^{k+1}).\tag{13}$$

We will also use other implicit methods in the examples below; see Appendix. Note that they are more costly since they lead to nonlinear equations such as (13) for θ^{k+1} that have to be solved at each time step.

We stress that the adaptive nature of our Neural Galerkin approach is different from time-space collocation methods based on neural networks [4, 21, 17] and other DNN-based PDE solution methods that are formulated over equidistant time steps [10].

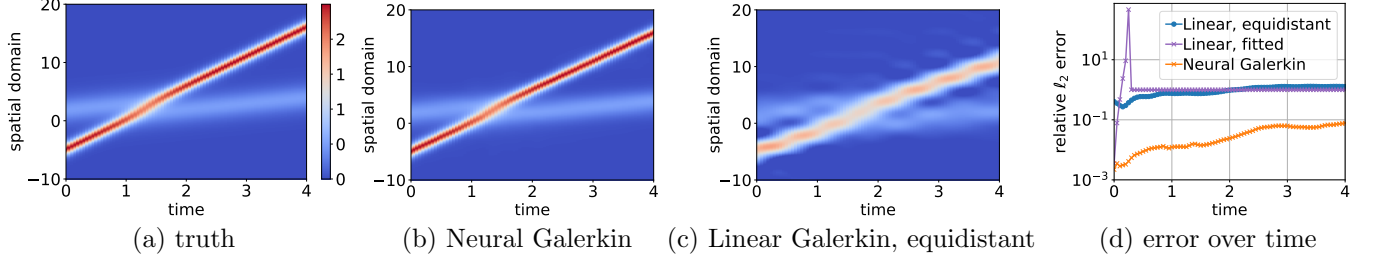


Figure 1.: Korteweg-De Vries: Neural Galerkin integrates in time a nonlinear parametrization of the solution and so obtains an accurate approximation with few degrees of freedom in this example. In contrast, linear (standard) Galerkin that derives approximations in fixed spaces with fixed bases without feature adaptation leads to poor approximations when there are local dynamics in the spatial domain as in this example.

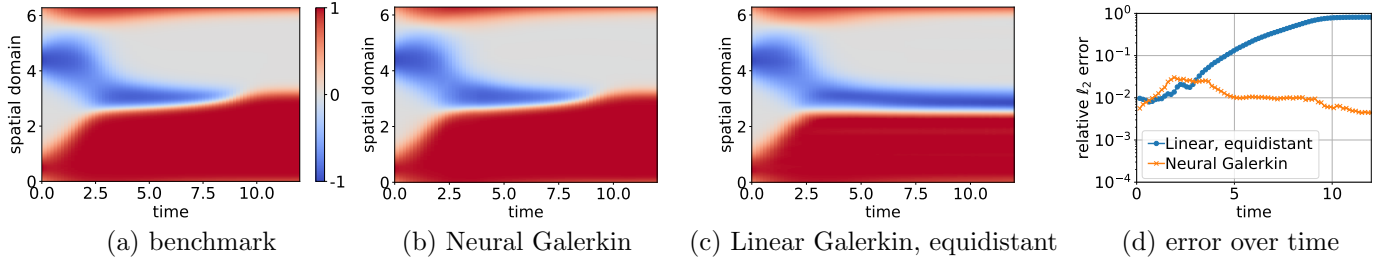


Figure 2.: Allen-Cahn: The proposed Neural Galerkin approach with a three-hidden-layer network correctly predicts the dynamics of the sharp walls that eventually separate the solution into two flat pieces at 0 and +1 in this experiment. In contrast, linear Galerkin with the same number of degrees of freedom wrongly predicts a solution with three flat pieces at $-1, 0$, and $+1$ because of the lack of expressiveness of the linear approximation.

Instead of deriving the variational formulation (4) in continuous time and then discretizing the Euler-Lagrange equations (6), one could also first discretize in time and then derive the Euler-Lagrange equation of the discrete-in-time optimization problem; this is similar to the distinction between discretize-then-optimize versus optimize-then-discretize approaches used e.g. in inverse problems and PDE-constrained optimization: see e.g. Ref. [9].

2.4. Neural architectures

Our method offers the possibility to use DNNs of arbitrary complexity and sophistication for the parametrization $U(\theta, \mathbf{x})$, in a way that can be tailored to known properties or symmetries of the solution of Eq. (1), as well as its boundary conditions. In our numerical experiments, we use two specific neural architectures. The first is a shallow (one-hidden-layer) network with m nodes given by

$$U(\theta, \mathbf{x}) = \sum_{i=1}^m c_i \varphi(\mathbf{x}, w_i, \mathbf{b}_i), \quad (14)$$

where θ is defined as $\theta = (c_i, w_i, \mathbf{b}_i)_{i=1}^m$ and $c_i, w_i \in \mathbb{R}$ and $\mathbf{b}_i \in \mathbb{R}^d$ are the parameters of the DNN, and $\varphi : \mathcal{X} \times \mathbb{R}^{d+1}$ is one of the following two nonlinear units (activation function): The first is the Gaussian kernel

$$\varphi_G(\mathbf{x}, w, \mathbf{b}) = \exp(-w^2 |\mathbf{x} - \mathbf{b}|^2), \quad (15)$$

which we use when $\mathcal{X} = \mathbb{R}^d$; the second is

$$\varphi_G^L(\mathbf{x}, w, \mathbf{b}) = \exp(-w^2 |\sin(\pi(\mathbf{x} - \mathbf{b})/L)|^2), \quad (16)$$

which we use when $\mathcal{X} = L\mathbb{T}^d$ with $L > 0$ and we need to enforce periodicity. Here and below the exponential function, sine and tanh act componentwise, and we refer to the $c_i(t)$ as the coefficients of the network and to the $w_i(t), \mathbf{b}_i(t)$ as its features.

The other neural architecture that we use is a feedforward neural network with $\ell \in \mathbb{N}$ hidden layers and m nodes per layer:

$$U(\theta, \mathbf{x}) = \mathbf{c}(t)^T \tanh(\mathbf{W}_\ell \tanh(\mathbf{W}_{\ell-1}(\cdots \varphi_{\tanh}^L(\mathbf{x}, \mathbf{W}_1, \mathbf{b}_1) \cdots)) + \mathbf{b}_{\ell-1}) + \mathbf{b}_\ell), \quad (17)$$

where $\theta = (\mathbf{c}, \mathbf{W}_1, \dots, \mathbf{W}_\ell, \mathbf{b}_1, \dots, \mathbf{b}_\ell)$ with $\mathbf{c} \in \mathbb{R}^m$, $\mathbf{W}_i \in \mathbb{R}^{m \times d}$, and $\mathbf{b}_i \in \mathbb{R}^d$ are the parameters, and φ_{\tanh}^L is the nonlinear unit

$$\varphi_{\tanh}^L(\mathbf{x}, \mathbf{W}, \mathbf{b}) = \tanh(\mathbf{W} \sin(2\pi(\mathbf{x} - \mathbf{b})/L)). \quad (18)$$

3. Numerical experiments

3.1. Korteweg-de Vries equation

Consider the KdV equation $\partial_t u + \partial_x^3 u - 6u\partial_x u = 0$ on the one-dimensional spatial domain $\mathcal{X} = [-20, 40] \subset \mathbb{R}$ with periodic boundary condition. We follow the setup described in Ref. [22], which for the initial conditions described in their Section I-a-(ii) leads to a solution of the KdV equation that consists of two interacting solitons that approach each other, collide, and then separate—this solution, shown in Figure 1(a), is available analytically, thereby providing us with a benchmark of the numerical results.

For the parametric solution, we use the shallow neural network defined in Eq. (14) with the Gaussian units defined in Eq. (16) and $m = 10$ nodes. Because the dimension of the spatial domain is one in this example, we simply take $d\nu_\theta(x) = dx$, and sample $n = 1000$ points uniformly in $[0, 1]$ to estimate M and F , without regularizing \tilde{M} . The initial parameter θ_0 is obtained via a least-squares fit of the initial condition. As integrator, we use RK45 so that the time-step size is adaptively chosen based on the dynamics of the solution.

The time-space plot of the Neural Galerkin approximation shown in Figure 1(b) is in close agreement with the analytic solution shown in Figure 1(a). The relative ℓ_2 error remains low over time, as shown in Figure 1(d). To emphasize the importance of the nonlinear feature adaptation, we also consider linear approximations given Eq. (14) with $m = 30$ nodes but with fixed features w_i , and \mathbf{b}_i that are either located equidistantly in \mathcal{X} or fitted to the initial condition and then kept fixed. In both cases, the linear approximation has the same number of degrees of freedom as the nonlinear Neural Galerkin approximation. The linear approximation leads to large errors that develop after only a few time steps, as apparent from the solution shown in Figure 1(c). This is also in agreement with Figure 1(d) which shows that the linear Galerkin approximations based on fixed features lead to errors that are orders of magnitude larger than the Neural Galerkin with the same number of degrees of freedom.

3.2. Allen-Cahn (AC) equation

Consider the prototypical reaction diffusion equation known as the AC equation

$$\partial_t u = \epsilon \partial_x^2 u - a(t, x)(u - u^3),$$

in the one-dimensional domain $\mathcal{X} = [0, 2\pi]$ with periodic boundary conditions. We set $\epsilon = 5 \times 10^{-2}$ in the diffusion term and let the coefficient in the reaction term vary in time and space using $a(t, x) = 1.05 + t \sin(x)$. This coefficient drives u towards $u = \pm 1$ for $t < 1.05$, whereas for $t > 1.05$ the solution u is driven towards ± 1 for x in the region where $\sin(x) < 1.05/t$ and 0 in the region where $\sin(x) > 1.05/t$; as $t \rightarrow \infty$ these two regions converge to $(0, \pi)$ and $(\pi, 2\pi)$, respectively. As initial condition we take

$$u(0, x) = \varphi_G^L(x, 400, 1/2) - \varphi_G^L(x, 400, 4.4),$$

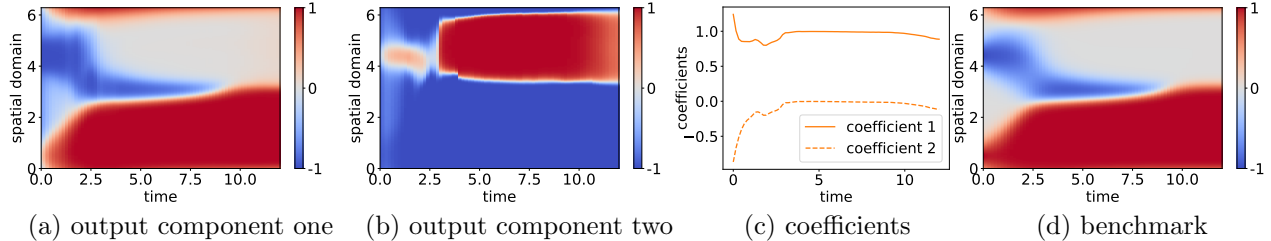


Figure 3.: Allen-Cahn: The plots visualize how Neural Galerkin propagates forward in time the coefficients and features of a DNN parametrization by following the dynamics prescribed by the PDE. Notice that the output components, defined in Eq. (19) and shown in (a) and (b), reflect the transition of the sharp walls between the flat pieces of the solution and that the dynamics rapidly change from time $t = 1.05$ to about $t = 2.5$ when the potential changes sign in parts of the spatial domain.

with φ_G^L defined in Eq. (16) and $L = 1/2$.

Figure 2(a) shows a benchmark solution computed with a grid-based method; see Section E in the Appendix for details. The solution consists of relatively flat pieces separated by sharp walls, which evolve in a way that is consistent with the evolving sign structure of the coefficient $a(t, x)$ described above. Figure 2(b) shows the Neural Galerkin solution obtained with the three-hidden-layer network defined in (17), with $m = 2$ tanh units (16 degrees of freedom) and fixed uniform measure $d\nu_\theta(x) = dx$. The time integration scheme is backward Euler with time-steps size $\delta t = 10^{-2}$. The corresponding optimization problem in each time step is approximately solved with SGD and $n = 1000$ samples to estimate M and F . As can be seen, the Neural Galerkin solution agrees well with the benchmark solution. In contrast, the solution obtained with linear Galerkin with 16 equidistantly located Gaussian basis functions defined in (16) shown in Figure 2(c) leads to a poorer approximation. This is further quantified in Figure 2(d) which shows that the Neural Galerkin solution with a three-hidden-layer network achieves an ℓ_2 error that is two orders of magnitude lower than that of the linear Galerkin solution.

Figure 3 visualizes the adaptation of the coefficients and features of the Neural Galerkin solution. Consider the network (17) with $\mathbf{c}(t) = (c_1(t), c_2(t))^T \in \mathbb{R}^2$, $\ell = 3$, and set

$$\psi_i(t, \mathbf{x}) = \mathbf{e}_i^T \tanh(\mathbf{W}_3(t) \tanh(\mathbf{W}_{2-1}(t) (\varphi_{\tanh}^L(\mathbf{x}, \mathbf{W}_1(t), \mathbf{b}_1(t)))) + \mathbf{b}_2(t) + \mathbf{b}_3(t)), \quad (19)$$

where $\mathbf{e}_i \in \mathbb{R}^2$ with $i = 1, 2$ are the two canonical unit vectors. Thus the output components $\psi_1(t, \mathbf{x})$ and $\psi_2(t, \mathbf{x})$ are weighted by the coefficients $c_1(t)$ and $c_2(t)$ to obtain the Neural Galerkin solution; these two components are shown in Figure 3(a) and (b). The corresponding coefficients are visualized in panel (c) and the benchmark solution is plotted again in panel (d). Even though the Neural Galerkin solution uses only two $\psi_i(t, \mathbf{x})$, because these functions depends nonlinearly on parameters that evolve in time, they adapt their shape to accurately approximate the solution.

3.3. Advection in unbounded, high-dimensional domains

Our next example is an advection equation in high dimension,

$$\partial_t u + \mathbf{a}(t, \mathbf{x}) \cdot \nabla_{\mathbf{x}} u = 0, \quad u(0, \mathbf{x}) = u_0(\mathbf{x}), \quad (20)$$

where $\mathbf{x} \in \mathcal{X} \equiv \mathbb{R}^d$, $\mathbf{a} : [0, \infty) \times \mathbb{R}^d \rightarrow \mathbb{R}^d$ is some bounded velocity field that is assumed to be differentiable in both its arguments, and $u_0 : \mathbb{R}^d \rightarrow \mathbb{R}$ is some initial condition satisfying $\lim_{|\mathbf{x}| \rightarrow \infty} u_0(\mathbf{x}) = 0$. This equation can in principle be solved by the method of characteristics, i.e. by considering

$$\dot{\mathbf{X}}(t, \mathbf{x}) = \mathbf{a}(t, \mathbf{X}(t, \mathbf{x})), \quad \mathbf{X}(0, \mathbf{x}) = \mathbf{x}, \quad (21)$$

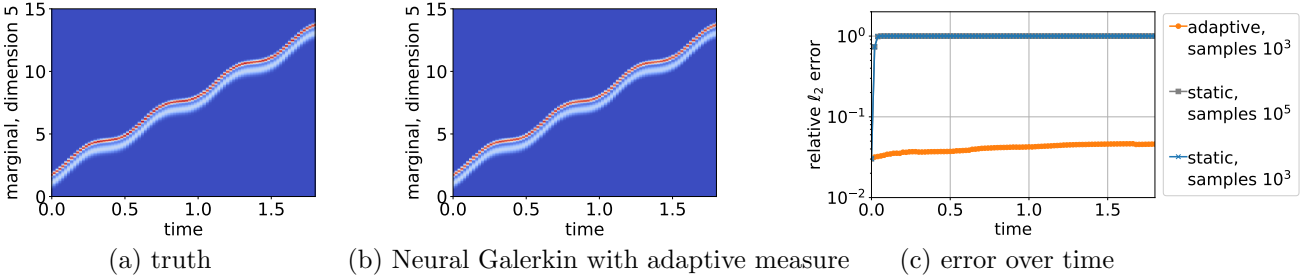


Figure 4.: High-dimensional advection with time-only varying advection speed: (a) marginal in dimension 5 of the analytic solution; (b) result of the Neural Galerkin method that adaptively samples data over time to estimate the operators M and F depending on the dynamics of the problem at hand. This is in stark contrast to classical time-space collocation approaches that uniformly sample over space and time when optimizing for a solution. In this example, the adaptive sampling is key for Neural Galerkin to accurately predict the local-in-space dynamics of the solution. In contrast, an approximate solution obtained with uniform sampling that is static over time fails to lead to meaningful predictions, as shown by the error plotted in (c).

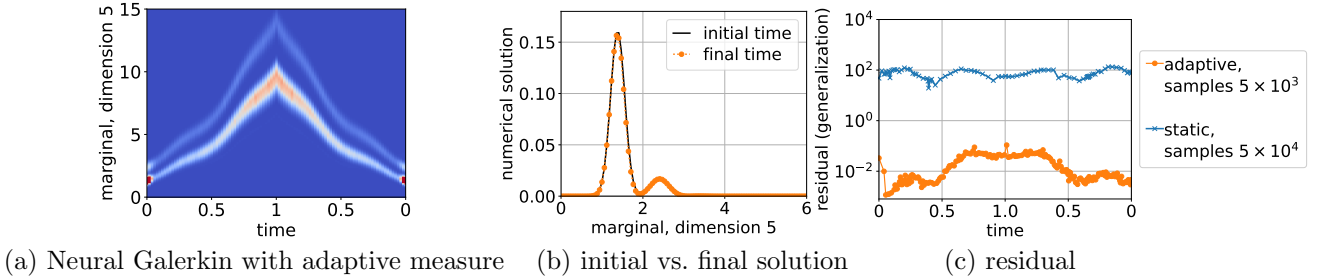


Figure 5.: High-dimensional advection with time-space varying advection speed: The equation is integrated forward in time until $t = 1$ and then integrated backwards until time $t = 0$, where the initial condition is reached again. Plot (a) shows the prediction of the Neural Galerkin method. Plot (b) shows that the Neural Galerkin solution at final time closely matches the initial condition, which means that little error is accumulated by integrating forward and then backward in time. Adaptive sampling is key in this example because the solution is local in the high-dimensional spatial domain. Neural Galerkin with adaptive sampling tracks the local dynamics well, whereas approximations based on static sampling fail after only a few time steps as shown by a large residual in (c).

and using

$$u(t, \mathbf{x}) = u_0(\mathbf{X}(-t, \mathbf{x})). \quad (22)$$

In practice, however, Eq. (22) is hard to use to obtain global information about the solution, except in situations where Eq. (21) can be solved explicitly (an instance of which we will also consider below as benchmark). Next we show how to numerically solve (20) directly using a Neural Galerkin scheme.

Advection with a time-dependent coefficient

In the first experiment with the advection equation, we make the transport coefficient depend only on time using

$$\mathbf{a}_t(t) = \mathbf{a}_s \odot (\sin(\mathbf{a}_v \pi t) + 5/4) \quad (23)$$

with $\mathbf{a}_s = [1, 2, \dots, d]^T$, $\mathbf{a}_v = 2 + \frac{2}{d}[0, 1, \dots, d-1]^T$ and the element-wise vector multiplication \odot . We set $d = 5$ and take as initial condition u_0 a mixture of two non-isotropic Gaussian packets, see Section F in the Appendix. In this case, the solution (22) can be derived explicitly, and we will use it as benchmark: its marginal in dimension five is shown in Figure 5(a); see also Figure 10 in the Appendix.

For Neural Galerkin, see Figure 5(b), we use a shallow network as in Eq. (14) with the exponential unit (15)—notice that since these units are isotropic, several of them are required to accurately approximate both the initial condition and the solution of Eq. (20) at time $t > 0$. We take $m = 50$ nodes and use the adaptive RK45 method as time-integrator. We also use a measure ν_θ adapted to the solution to sample $n = 1000$ data points $\{\mathbf{x}_i\}_{i=1}^n$ at each integration step to estimate M and F via Eq. (11). Specifically, we take ν_θ to be the Gaussian mixture with 50 nodes obtained from the current neural approximation of the solution by equating the weights c_i , dividing w_i by a factor $\kappa > 0$, and keeping the same \mathbf{b}_i , i.e. if the current Neural Galerkin approximation of the solution is

$$U(\theta, \mathbf{x}) = \sum_{i=1}^{50} c_i(t) \exp(-w_i^2(t)|\mathbf{x} - \mathbf{b}_i(t)|^2), \quad (24)$$

we sample the data points from

$$d\nu_{\theta(t)}(\mathbf{x}) = C^{-1} \sum_{i=1}^{50} \exp(-\frac{1}{\kappa^2} w_i^2(t)|\mathbf{x} - \mathbf{b}_i(t)|^2) d\mathbf{x}, \quad (25)$$

where C is a normalization constant and $\kappa = 1$ in this experiment. Using this adapted measure is key for accuracy, and leads to the small ℓ_2 error plotted in Figure 4(c). If instead we estimate M and F by drawing the data points uniformly in $[0, 15]^d$ (to cover the domain over which the solution propagates for $t \in [0, 2]$), the relative error is 100% after only a few time steps even if we use as many as $n = 10^5$ data points, see Figure 4(c). This emphasizes the importance of using adaptivity in both the function approximation via neural networks, and the data acquisition to estimate M and F . This double-adaptivity is a key distinguishing feature of the proposed Neural Galerkin scheme compared to existing DNN approaches.

Advection with time- and space-dependent coefficients

Next we consider Eq. (20) with the time-space varying advection speed,

$$\mathbf{a}_{st}(t, \mathbf{x}) = \mathbf{a}_s \odot (\sin(\mathbf{a}_v \pi t) + 3) \odot (\mathbf{x} + 1)/10, \quad (26)$$

where $\mathbf{a}_s, \mathbf{a}_v$ are the vectors defined in Eq. (23). For the initial condition we take a sum of two Gaussian packets, see Section F in the Appendix for details. Since the analytic solution for this problem is not available in closed form, to assess the performance of our Neural Galerkin scheme, we numerically integrate the problem forward in time until time $T = 1$, then invert the advection coefficient in time, and integrate backwards until time 0: we can then estimate the error by comparing the final numerical solution with the initial condition. The numerical setup is the same as in the previous experiment with the advection speed (23), except that we draw $n = 5000$ samples from the adapted measure in (25) at each integration

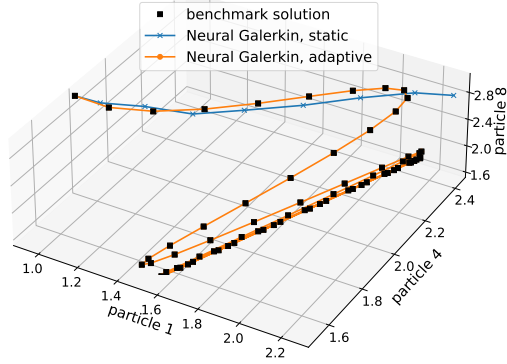


Figure 6.: Particles in harmonic trap: As the particles become attracted by the trap, the particle density becomes increasingly concentrated in the high-dimensional domain. The Neural Galerkin scheme adaptively samples from the neural approximation of the density over time and thereby accurately tracks the particles mean position (orange) in contrast to methods with static sampling done uniformly in the spatial domain (blue).

step to estimate M and F . Figure 5(a) shows the time-space marginal of the Neural Galerkin solution: as can be seen the spatially varying coefficient leads to a significantly changing solution over time. Figure 5(b) compares the initial condition with the final solution obtained by integrating forward and then backward in time, which are in good agreement. In Figure 5(c) we show an estimate of the PDE residual defined in Eq. (5) using the adapted measure in (25) and estimated using 10^5 samples drawn independently from this measure. The residuals indicate that the proposed Neural Galerkin approach with adaptive sampling approximates well the local dynamics in this high-dimensional transport problem, whereas static sampling with a uniform distribution fails again to provide meaningful predictions.

3.4. Fokker-Planck equations in high-dimension

Let $\mathcal{X} = \mathbb{R}^d$ and consider the evolution of d interacting particles with positions $X_1(t), \dots, X_d(t) \in \mathbb{R}$ governed by

$$dX_i = g(t, X_i)dt + \sum_{j=1}^d K(X_i, X_j)dt + \sqrt{2D} dW_i, \quad (27)$$

with $i = 1, \dots, d$ and where $g : [0, \infty) \times \mathbb{R} \rightarrow \mathbb{R}$ is a time-dependent one-body force, $K : \mathbb{R} \times \mathbb{R} \rightarrow \mathbb{R}$ a pairwise interaction term, $D > 0$ the diffusion coefficient, and W_i are independent Wiener processes. The evolution of the joint probability density of these particles, $u(t, \mathbf{x})$ with $\mathbf{x} = [x_1, \dots, x_d]^T$, is governed by the Fokker-Planck equation

$$\partial_t u = \sum_{i=1}^d (-\partial_{x_i} (u h_i(t, x_1, \dots, x_d)) + D \partial_{x_i}^2 u), \quad (28)$$

where $h_i(t, x_1, \dots, x_d) = g(t, x_i) + \sum_{j=1}^d K(x_i, x_j)$. In high dimension, one typically resorts to Monte Carlo methods based on integrating Eq. (27) to obtain samples from the density u . In contrast, we solve the Fokker-Planck equation (28) directly with our Neural Galerkin scheme to derive an approximation of $u(t, \mathbf{x})$ via $U(\theta(t), \mathbf{x})$ everywhere in the domain \mathcal{X} . Having the density at hand allows us to efficiently compute quantities of interest that are not expressible as expectation over u , such as the entropy, and therefore not directly accessible to Monte Carlo methods. Note that the Neural Galerkin scheme also involves sampling to estimate M and F , but it is done adaptively based on the current neural solution to keep low the number of samples required to obtain accurate estimates.

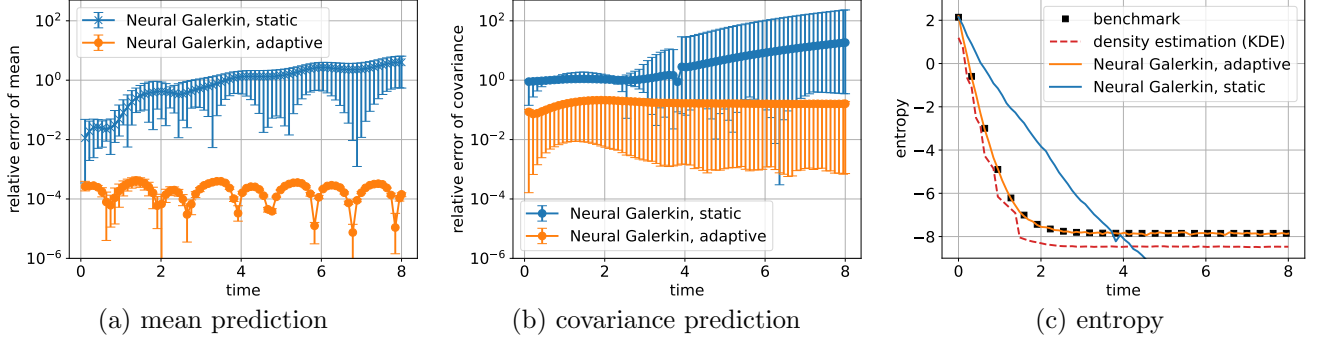


Figure 7.: Particles in harmonic trap: The Neural Galerkin scheme with adaptive sampling achieves orders of magnitude lower errors in predicting the mean (orange, panel a) and the covariance (orange, panel b) of the particle density than methods that rely on static sampling uniform over time and space (blue, panels a and b). Additionally, the Neural Galerkin scheme provides an approximation of the particle density that allows efficiently computing quantities of interest such as the entropy (panel c), in contrast to Monte Carlo that only draws samples of the particle distribution. Panel (c) also shows the estimate of the entropy obtained with kernel density estimation (KDE) (red dashed).

Particles in harmonic trap

In the following experiment, we set

$$g(t, x) = a(t) - x, \quad K(x, y) = \frac{\alpha}{d}(y - x) \quad (29)$$

with $a : [0, \infty) \rightarrow \mathbb{R}$ and $\alpha > 0$. This corresponds to following the evolution of d particles put in a harmonic trap centered around the moving position $[a(t), \dots, a(t)]^T \in \mathcal{X}$ and also attracting each other harmonically. This choice has the advantage that we can derive closed ODEs for the mean and covariance of the particle positions that can be solved numerically and used as benchmark, see Section G in the Appendix for details. If the initial condition $u(0, \mathbf{x})$ is a Gaussian probability density, the density $u(t, \mathbf{x})$ remains Gaussian for all times t , with the mean and covariance given by the ODEs. Accordingly, we take $u(0, \mathbf{x})$ to be an isotropic Gaussian density with mean $9/10 + 21/(10(d-1))[0, 1, \dots, d-1]^T$ and variance $\sigma^2 = 0.1$. We take $d = 8$ particles and set $a(t) = 5/4(\sin(\pi t) + 3/2)$, $\alpha = 1/4$ and $D = 10^{-2}$.

We apply our Neural Galerkin scheme to solve the Fokker-Planck equation (28) using the neural network defined in (14) with $m = 30$ nodes and non-negative weights to guarantee that the Neural Galerkin solution is non-negative; see Section G in the Appendix for details. We use implicit Euler with time-step size $\delta t = 10^{-3}$. The number of SGD iterations to solve Eq. (13) in θ^{k+1} is 5×10^3 . To estimate M and F , we draw $n = 1000$ samples at every time-step, using the adaptive sampling procedure used in the previous experiments with the advection equation. Figure 6 shows the mean position of particles 1, 4, and 8 in the spatial domain over time. The approximation obtained with Neural Galerkin with adaptive sampling closely follows the benchmark solution. In contrast, estimation of M and F via uniform sampling in $[0, 5]^d$ leads again to a poor approximation. The relative error of the predicted mean with adaptive Neural Galerkin is roughly 10^{-4} as shown in Figure 7(a) and the entries of the covariance matrix are approximated with relative error of about 10^{-1} to 10^{-2} as shown in Figure 7(b). Because Neural Galerkin provides an approximation of the density of the particles, rather than just samples of their positions as Monte Carlo methods, we can compute the entropy of the particle distribution over time; see Figure 7(c). The adaptive Neural Galerkin approximation of the entropy is in close agreement with the benchmark, whereas static sampling and Monte Carlo combined with density estimation from 5,000 samples leads to poor approximations.

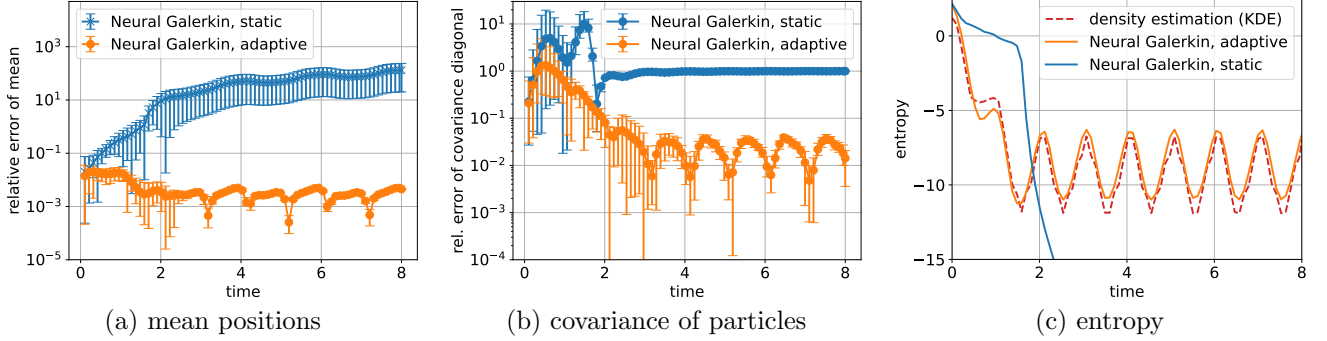


Figure 8.: Particles in aharmonic trap: We use the same plotting convention as in Figure 7

Particles in aharmonic trap

Next we consider an aharmonic trap with one-body force $g(t, X_i) = (a(t) - x)^3$ and the same pairwise interaction term K as defined in Eq. (29) except that α is set to $\alpha = -0.5$, so that the particles now repel each other within the attracting trap. Because of the nonlinear force, the density u is not necessarily Gaussian anymore. A Monte Carlo estimate of the particle positions from 100,000 samples serves as benchmark in the following.

To apply the Neural Galerkin scheme in this experiment, we take the neural network defined in Eq. (14) with $m = 40$ nodes and non-negative weights. Time is discretized with implicit Euler and $\delta t = 10^{-3}$. We take $n = 5000$ sample and 1000 SGD iterations in each time step. The rest of the setup is the same as in the example with the harmonic trap. Figure 8(a) and (b) show the relative error of the mean and the relative error of the covariance diagonal, respectively. With adaptive sampling, the Neural Galerkin scheme achieves an error between 10^{-3} and 10^{-2} . In contrast, static sampling is insufficient and leads to large relative errors. Note that the off-diagonal elements of the covariance of the particle density converge to zero over time in this experiment and thus the relative error is not informative and not plotted here. Because the Neural Galerkin scheme provides an approximation of the density of the particles, we can efficiently compute the entropy: As shown in Figure 8(c), it is in agreement with the prediction obtained with Monte Carlo and density estimation from 100,000 samples.

4. Concluding remarks

As machine-learning techniques via deep learning play an ever more important role in enabling realistic simulations of phenomena and processes in science and engineering, there is an increasing need for training on data that are informative about the underlying physics. This problem of data generation becomes especially important in dynamical systems that evolve over time where *a priori* data is sparse or non-existent, and static data collection in a pre-processing step is insufficient. Our Neural Galerkin scheme is one proposal for intertwining data acquisition and numerical simulations in an adaptive way. The scheme learns PDE solutions by evolving a non-linear function representation, which is adjusted from data points obtained via importance sampling that is informed by the solution itself. Our numerical experiments demonstrate that the adaptivity in function approximation as well as data collection is key to enable accurate prediction of local features in high-dimensional domains.

These results suggest that the proposed Neural Galerkin scheme can be applied to simulate many other high-dimensional equations relevant in science and engineering, such as kinetic equations, non-linear Fokker-Planck equations, Boltzmann equations, etc. This would be especially useful in situations where Monte-Carlo methods are not directly applicable because the solution does not admit a representation via the Feynman-Kac formula. The usage of the neural Galerkin scheme in such applications also opens the door

to several interesting questions that we leave as future research avenues: First, we should understand better which structural properties of the neural architectures will guarantee that the function approximation from (2) $u(t, \mathbf{x}) \approx U(\theta(t), \mathbf{x})$ will hold uniformly in time. For some initial efforts in the context of shallow ReLU architectures we refer the reader to [25]. Second, we should quantify when the integral defining the instantaneous loss (5) admits an efficient estimation, beyond what non-adaptive Monte-Carlo schemes can provide, by exploiting sparsity of the residual in a certain domain, not necessarily the spatial domain. For example, if the solution is represented in the frequency domain, then locality (often referred to as sparsity) means that only few frequencies are relevant, which in principle can be exploited numerically with the Neural Galerkin scheme by using suitable nonlinear parametrizations. Third, it would be interesting to explore and systematize importance sampling strategies that adapt to the transient regularity structures appearing in the solution and thereby will allow us to maintain an adaptive neuron budget. Such strategies could for example use birth-death processes [18], which would allow us to vary the width of the neural network in time, or methods that couple the PDE to some evolution equation for the input data points used to sample the residual.

Acknowledgments

B.P. was partially supported by NSF under award DMS-2046521 and IIS-1901091 and the Air Force Center of Excellence on Multi-Fidelity Modeling of Rocket Combustor Dynamics under Award Number FA9550-17-1-0195.

References

- [1] Y. Bar-Sinai, S. Hoyer, J. Hickey, and M. P. Brenner. Learning data-driven discretizations for partial differential equations. *Proceedings of the National Academy of Sciences*, 116(31):15344–15349, 2019.
- [2] J. Berg and K. Nyström. A unified deep artificial neural network approach to partial differential equations in complex geometries. *Neurocomputing*, 317:28 – 41, 2018.
- [3] K. Bhattacharya, B. Hosseini, N. B. Kovachki, and A. M. Stuart. Model reduction and neural networks for parametric PDEs. *The SMAI journal of computational mathematics*, 7:121–157, 2021.
- [4] M. W. M. G. Dissanayake and N. Phan-Thien. Neural-network-based approximations for solving partial differential equations. *Communications in Numerical Methods in Engineering*, 10(3):195–201, 1994.
- [5] J. Dormand and P. Prince. A family of embedded Runge-Kutta formulae. *Journal of Computational and Applied Mathematics*, 6(1):19–26, 1980.
- [6] Y. Du and T. A. Zaki. Evolutional deep neural network. *Phys. Rev. E*, 104:045303, Oct 2021.
- [7] W. E, J. Han, and A. Jentzen. Deep learning-based numerical methods for high-dimensional parabolic partial differential equations and backward stochastic differential equations. *Communications in Mathematics and Statistics*, 5(4):349–380, Dec 2017.
- [8] A. Ern and J.-L. Guermond. *Theory and practice of finite elements*. Springer, 2004.
- [9] M. D. Gunzburger. *Perspectives in Flow Control and Optimization*. Society for Industrial and Applied Mathematics, 2002.
- [10] J. Han, A. Jentzen, and W. E. Solving high-dimensional partial differential equations using deep learning. *Proceedings of the National Academy of Sciences*, 115(34):8505–8510, 2018.

- [11] Y. Khoo, J. Lu, and L. Ying. Solving for high-dimensional committor functions using artificial neural networks. *Research in the Mathematical Sciences*, 6(1):1, Oct 2018.
- [12] Y. Khoo, J. Lu, and L. Ying. Solving parametric PDE problems with artificial neural networks. *European Journal of Applied Mathematics*, 23:421–435, 2020.
- [13] D. Kochkov, J. A. Smith, A. Alieva, Q. Wang, M. P. Brenner, and S. Hoyer. Machine learning–accelerated computational fluid dynamics. *Proceedings of the National Academy of Sciences*, 118(21), 2021.
- [14] N. B. Kovachki, Z. Li, B. Liu, K. Azizzadenesheli, K. Bhattacharya, A. M. Stuart, and A. Anandkumar. Neural operator: Learning maps between function spaces. *arXiv*, 2108.08481, 2021.
- [15] K. Lee and K. T. Carlberg. Model reduction of dynamical systems on nonlinear manifolds using deep convolutional autoencoders. *Journal of Computational Physics*, 404:108973, 2020.
- [16] A. Rahimi and B. Recht. Random features for large-scale kernel machines. In J. Platt, D. Koller, Y. Singer, and S. Roweis, editors, *Advances in Neural Information Processing Systems*, volume 20. Curran Associates, Inc., 2008.
- [17] M. Raissi, P. Perdikaris, and G. Karniadakis. Physics-informed neural networks: A deep learning framework for solving forward and inverse problems involving nonlinear partial differential equations. *Journal of Computational Physics*, 378:686–707, 2019.
- [18] G. Rotskoff, S. Jelassi, J. Bruna, and E. Vanden-Eijnden. Global convergence of neuron birth-death dynamics. *arXiv*, 1902.01843, 2019.
- [19] G. M. Rotskoff, A. R. Mitchell, and E. Vanden-Eijnden. Active importance sampling for variational objectives dominated by rare events: Consequences for optimization and generalization. *arXiv*, 2008.06334, 2021.
- [20] S. H. Rudy, J. Nathan Kutz, and S. L. Brunton. Deep learning of dynamics and signal-noise decomposition with time-stepping constraints. *Journal of Computational Physics*, 396:483–506, 2019.
- [21] J. Sirignano and K. Spiliopoulos. DGM: A deep learning algorithm for solving partial differential equations. *Journal of Computational Physics*, 375:1339–1364, 2018.
- [22] T. R. Taha and M. I. Ablowitz. Analytical and numerical aspects of certain nonlinear evolution equations. III. Numerical, Korteweg-de Vries equation. *Journal of Computational Physics*, 55(2):231–253, 1984.
- [23] Q. Wang, J. S. Hesthaven, and D. Ray. Non-intrusive reduced order modeling of unsteady flows using artificial neural networks with application to a combustion problem. *Journal of Computational Physics*, 384:289–307, 2019.
- [24] Q. Wang, N. Ripamonti, and J. S. Hesthaven. Recurrent neural network closure of parametric POD-Galerkin reduced-order models based on the Mori-Zwanzig formalism. *Journal of Computational Physics*, 410:109402, 2020.
- [25] S. Wojtowytsch and W. E. Some observations on high-dimensional partial differential equations with Barron data. In *Mathematical and Scientific Machine Learning*, 2021.

A. Learning in the Banach space \mathcal{F}_1

Let us consider the Neural Galerkin representation $u(t, \mathbf{x}) = U(\theta(t), \mathbf{x})$ in a situation where θ is infinite dimensional, namely when

$$u(t, \mathbf{x}) = \int_{\mathcal{Z}} \phi(\mathbf{x}, z) d\gamma_t(z) \quad (30)$$

where $\phi : \mathcal{X} \times \mathcal{Z} \rightarrow \mathbb{R}$ is some nonlinear unit (like e.g. the ReLU), and γ_t is a Radon measure with finite total variation defined on \mathcal{Z} : we will denote the space of such Radon measures by $\mathcal{M}(\mathcal{Z})$. Functions of the type defined in Eq. (30) form a Banach space in which the norm of $u(t)$ is the minimum total variation of γ_t among all Radon measures consistent with Eq. (30); these function can also be approximated by shallow (two-layer) neural networks, which converge to functions as defined in Eq. (30) in the limit of infinite width. In this context, one can specify the evolution of γ_t by requiring that

$$\dot{\gamma}_t \in \operatorname{argmin}_{\dot{\gamma} \in \mathcal{M}(\mathcal{Z})} \int_{\mathcal{X}} \left| \int_{\mathcal{Z}} \phi(\mathbf{x}, z) d\dot{\gamma}(z) - f(t, \mathbf{x}, \int_{\mathcal{Z}} \phi(\cdot, z) d\gamma_t(z)) \right|^2 d\nu(\mathbf{x}) \quad (31)$$

where ν is some positive measure on \mathcal{X} . The Euler-Lagrange equation associated with this minimization problem gives the evolution equation for γ_t :

$$\int_{\mathcal{Z}} M(z, z') d\dot{\gamma}_t(z') = F(t, z, \gamma_t) \quad (32)$$

where

$$\begin{cases} M(z, z') = \int_{\mathcal{X}} \phi(\mathbf{x}, z) \phi(\mathbf{x}, z') d\nu(\mathbf{x}), \\ F(t, z, \gamma) = \int_{\mathcal{X}} \phi(\mathbf{x}, z) f(t, \mathbf{x}, \int_{\mathcal{Z}} \phi(\cdot, z') d\gamma(z')) d\nu(\mathbf{x}). \end{cases} \quad (33)$$

B. Another derivation of the Neural Galerkin equation $M(\theta)\dot{\theta} = F(t, \theta)$

Let $u(t)$ be the solution of the PDE at time t and $U(\theta(t))$ be its parametric representation. In general we do not have access to $u(t)$ (except at initial time through the prescribed initial condition), but if we had an oracle giving us this solution one option to determine the parameters $\theta(t)$ would be to minimize an objective like

$$E(\theta(t)) = R(u(t), U(\theta(t))) \quad (34)$$

where $R : \mathcal{U} \times \mathcal{U} \rightarrow \mathbb{R}$ is such that (i) $R(u, v) \geq 0$ for all $u, v \in \mathcal{U}$; (ii) $R(u, u) = 0$ for all $u \in \mathcal{U}$ and (iii) $R(u, v)$ is strictly convex in v for all $u \in \mathcal{U}$. Assuming that $R(u, v)$ is twice differentiable in both its arguments, this requires that

$$\forall u \in \mathcal{U} \quad : \quad R(u, u) = 0, \quad D_v R(u, v)|_{v=u} = 0 \quad \text{and} \quad D_{v,v}^2 R(u, v)|_{v=u} \quad \text{is positive-definite} \quad (35)$$

where D denotes derivative in \mathcal{U} . Together with $R(u, u) = 0$, note that this also implies that $D_u R(u, v)|_{v=u} = 0$ for all $u \in \mathcal{U}$.

Suppose that the current solution $u(t)$ is representable exactly, i.e. there exists $\theta(t) \in \Theta$ such that $U(\theta(t)) = u(t)$. This implies that $E(\theta(t)) = 0$, and it is natural to require that this objective remains zero, or as close to zero as possible, as time evolves. With this in mind, we can use the following result:

Proposition 1. Assume that (i) $U(\theta(t)) = u(t)$ and (ii) the objective $R(u, v)$ satisfies the conditions (35), so that $E(\theta(t)) = 0$. Then

$$\lim_{h \rightarrow 0} h^{-2} E(\theta(t+h)) = \frac{1}{2} \dot{\theta}^T M(\theta(t)) \dot{\theta} + \dot{\theta} \cdot F(t, \theta(t)) + \frac{1}{2} b(t, \theta(t)) =: L(\dot{\theta}), \quad (36)$$

where

$$\begin{aligned}
M(\theta) &= \langle \nabla_{\theta} U(\theta), D_{v,v}^2 R(U(\theta), U(\theta)) \nabla_{\theta} U(\theta) \rangle \\
F(t, \theta) &= \langle f(t, U(\theta)), D_{u,v}^2 R(U(\theta), U(\theta)) \nabla_{\theta} U(\theta) \rangle \\
b(t, \theta) &= \langle f(t, U(\theta)), D_{u,u}^2 R(U(\theta), U(\theta)) f(t, U(\theta)) \rangle
\end{aligned} \tag{37}$$

Proof: A straightforward calculation using the conditions in (35) as well as $\partial_t u(t) = f(t, u(t)) = f(t, U(\theta(t)))$ indicates that

$$\begin{aligned}
E(\theta(t+h)) &= R(u(t+h), U(\theta(t+h))) \\
&= \frac{1}{2} h^2 \langle f(t, U(\theta(t))), D_{u,u}^2 R(U(\theta(t)), U(\theta(t))) f(t, U(\theta(t))) \rangle + \frac{1}{2} h^2 \langle \nabla_{\theta} U(\theta(t)) \cdot \dot{\theta}, D_{v,v}^2 R(U(\theta(t)), U(\theta(t))) \nabla_{\theta} U(\theta(t)) \rangle \\
&\quad + h^2 \langle f(t, U(\theta(t))), D_{u,v}^2 R(U(\theta(t)), U(\theta(t))) \nabla_{\theta} U(\theta(t)) \cdot \dot{\theta} \rangle + o(h^2)
\end{aligned} \tag{38}$$

Dividing by h^2 and taking the limit as $h \rightarrow 0$ establishes (36). \square

Minimizing the objective defined in Eq. (36) over $\dot{\theta}$ given $\theta(t)$ leads us back to an evolution equation for $\theta(t)$ that is structurally similar the Neural Galerkin equation derived in the main text, that is

$$M(\theta(t)) \dot{\theta}(t) = F(t, \theta(t)), \tag{39}$$

and is to be solved with the initial condition

$$\theta(0) \in \underset{\theta}{\operatorname{argmin}} R(u_0, U(\theta)). \tag{40}$$

In particular it is easy to see that if we take

$$R(u, v) = \int_{\mathcal{X}} |u(t, \mathbf{x}) - v(t, \mathbf{x})|^2 d\nu(\mathbf{x}), \tag{41}$$

then the system of ODEs defined in Eq. (39) is exactly the same system as the system of ODEs given in the main text with M and F given in Eq. (8) with $\nu_{\theta} = \nu$. The formulation above is however more general, and offers a principled way to specify the measure ν_{θ} . For example, for equations like the Fokker-Planck equation that evolve a probability density $u(t) > 0$ such that $\int_{\mathcal{X}} u(t, \mathbf{x}) d\mathbf{x} = 1$, it common objective is the Kullback-Leibler divergence

$$R(u, v) = \int_{\mathcal{X}} \log \left(\frac{u(\mathbf{x})}{v(\mathbf{x})} \right) u(\mathbf{x}) d\mathbf{x}. \tag{42}$$

With this choice we arrive at Eq. (39) with

$$\begin{aligned}
M(\theta) &= \int_{\mathcal{X}} \frac{\nabla_{\theta} U(\theta, \mathbf{x}) \otimes \nabla_{\theta} U(\theta, \mathbf{x})}{U(\theta, \mathbf{x})} d\mathbf{x} \\
F(t, \theta) &= \int_{\mathcal{X}} \frac{\nabla_{\theta} U(\theta, \mathbf{x}) f(t, \mathbf{x}, U(\theta))}{U(\theta, \mathbf{x})} d\mathbf{x}
\end{aligned} \tag{43}$$

These correspond to using $d\nu_{\theta}(\mathbf{x}) = |U(\theta, \mathbf{x})|^{-1} d\mathbf{x}$.

C. Comparison with global methods

Let us compare the Neural Galerkin equation we use with the equations one obtains by treating the problem globally in time, i.e. by putting the spatial and the temporal variables on the same footing as in the Deep Ritz method [4, 21, 17, 2]. An optimal trajectory (in the $L_2([0, T] \times \mathcal{X}, \nu_0)$ sense) in parameter space satisfies

$$\min_{\{\theta(t) \in \Theta; t \in [0, T]\}} \int_0^T J_t(\theta, \dot{\theta}(t)) dt, \tag{44}$$

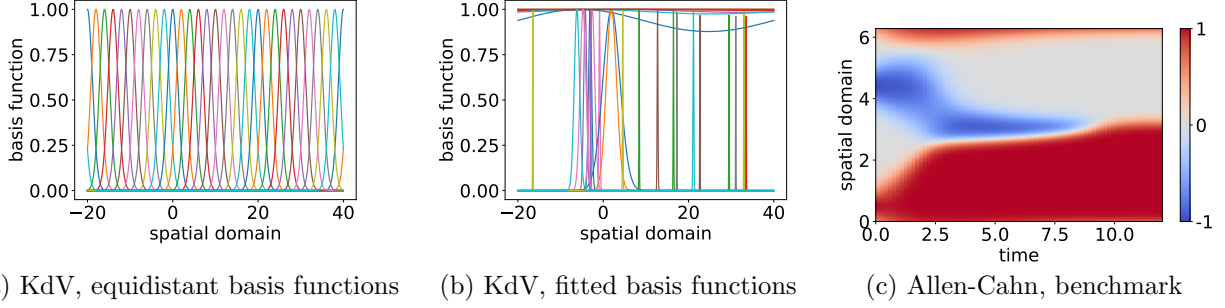


Figure 9.: KdV and Allen-Cahn: Basis functions used for linear Galerkin approximations and the time-space plot of the benchmark solution for the Allen-Cahn experiment.

subject to $\theta(0) = \theta_0$. The Euler-Lagrange equations associated with this minimization problem are

$$\frac{d}{dt} \partial_{\eta} J_t(\theta, \dot{\theta}) = \partial_{\theta} J_t(\theta, \dot{\theta}), \quad \theta(0) = \theta_0, \quad \partial_{\eta} J_T(\theta(T), \dot{\theta}(T)) = 0. \quad (45)$$

Explicitly, these read

$$\frac{d}{dt} \left(M(t, \theta) \dot{\theta} - F(t, \theta) \right) = H(t, \theta, \dot{\theta}), \quad \theta(0) = \theta_0, \quad M(T, \theta(T)) \dot{\theta}(T) = F(T, \theta(T)), \quad (46)$$

where we defined

$$H(t, \theta, \eta) = \int_{\mathcal{X}} (\nabla_{\theta} \nabla_{\theta} U(\theta, \mathbf{x}) \eta - \nabla_{\theta} U(\theta, \mathbf{x}) D_u f(t, \mathbf{x}, U(\theta))) (\nabla_{\theta} U(\theta, \mathbf{x}) \cdot \eta - f(t, \mathbf{x}, U(\theta))) d\nu_{t, \theta}(\mathbf{x}) \quad (47)$$

Eqs. (46) are a boundary value problem which is harder to solve than the Neural Galerkin Eq. (7).

D. Korteweg-De Vries (KdV) equation

The parameters of the network at time $t = 0$ are fitted to the initial condition via the least-squares loss function and ADAM optimization. Batch size is 10^5 and number of iterations is 10^5 . Samples are drawn uniformly in the spatial domain and the learning rate is 10^{-1} . We take five replicates with randomized initialization of parameters and then use the fit with lowest error on test samples.

The relative ℓ_2 error is computed as follows: Consider the $w = 2048$ equidistant grid points x_1, \dots, x_w in \mathcal{X} and define

$$\mathbf{u}(t) = [u(t, x_1), \dots, u(t, x_w)]^T \in \mathbb{R}^w,$$

to be the vector of the analytic solution u at time t and at the grid points x_1, \dots, x_w . Similarly, define $\tilde{\mathbf{u}}(t) = [\tilde{u}(t, x_1), \dots, \tilde{u}(t, x_w)]^T$ as the solution vector corresponding to an approximation \tilde{u} . Then, the reported relative ℓ_2 error is

$$e_{\ell_2} = \frac{\sum_{k=0}^K \|\mathbf{u}(t_k) - \tilde{\mathbf{u}}(t_k)\|_2^2}{\sum_{k=0}^K \|\mathbf{u}(t_k)\|_2^2}.$$

For linear Galerkin with equidistant basis functions, the basis functions are Gaussians units φ_G^L with a fixed bandwidth and equidistantly located in the domain Ω , see Figure 9a. For the comparison with linear Galerkin with basis functions fitted to the initial condition, we use the units fitted to the initial condition as described above and keep the features fixed, see Figure 9b.

E. Allen-Cahn (AC) equation

The benchmark solution is computed with a finite-difference discretization on 2048 equidistant grid points in the spatial domain. Time is discretized with semi-implicit Euler where the linear operators are treated implicitly and the nonlinear operators are treated explicitly. The time-step size is 10^{-5} . The time-space plot of the benchmark solution is shown in Figure 9c. The initial condition for the Neural Galerkin scheme is fitted analogously to fitting of the initial condition in the experiment with the KdV equation. Neural Galerkin uses a backward Euler discretization in time and then takes the gradient with automatic differentiation implemented in JAX (<https://github.com/google/jax>). The nonlinear system is solved with ADAM and 10,000 iterations.

Linear Galerkin is derived on equidistant Gaussian units analogously to the setup described for the numerical experiment with the KdV equation. The initial condition is fitted via a linear least-squares problem in case of linear Galerkin. Time is discretized with backward Euler, which leads to a nonlinear system at each time step. The nonlinear system is solved with ADAM analogously to how the nonlinear system of equations is solved in Neural Galerkin.

F. Advection in unbounded, high-dimensional domains

The initial condition is given by the probability density function of the mixture of two Gaussians with means

$$\boldsymbol{\mu}_1 = \frac{11}{10} \begin{bmatrix} 1 \\ 1 \\ \vdots \\ 1 \end{bmatrix}, \quad \boldsymbol{\mu}_2 = \frac{3}{4} \begin{bmatrix} 1.5 - (-1)^1 1/(d+1) \\ 1.5 - (-1)^2 2/(d+1) \\ \vdots \\ 1.5 - (-1)^d d/(d+1) \end{bmatrix}$$

and covariance matrices

$$\boldsymbol{\Sigma}_1 = \frac{1}{200} \begin{bmatrix} 2 & & & \\ & 4 & & \\ & & \ddots & \\ & & & 2d \end{bmatrix}, \quad \boldsymbol{\Sigma}_2 = \frac{1}{200} \begin{bmatrix} d & & & \\ & d-1 & & \\ & & \ddots & \\ & & & 1 \end{bmatrix}. \quad (48)$$

The parameters of the network at time $t = 0$ are fitted to the initial condition via a least-squares loss and ADAM, as in the previous experiments. The exact solution in case of the time-only varying coefficient is given by

$$u(t, \mathbf{x}) = u_0 \left(\mathbf{x} - \int_0^t \mathbf{a}_t(s) ds \right), \quad (49)$$

where \mathbf{a}_t is the time-varying coefficient defined in the main text.

Marginals of the solutions are computed as follows: Let $\mathcal{X} = \mathcal{X}_1 \times \dots \times \mathcal{X}_d$ be the domain of interest. We then plot for each dimension $i = 1, \dots, d$ the function

$$(t, x_i) \mapsto \int_{\Omega_1} \dots \int_{\Omega_{i-1}} \int_{\Omega_{i+1}} \dots \int_{\Omega_d} u(t, x_1, \dots, x_{i-1}, x_{i+1}, \dots, x_d),$$

where u is the function of which marginals are to be plotted and the integrals are numerically approximated via Monte Carlo and 8192 samples. The samples are drawn from the analytic solution, which is available in this experiment. The marginals for all five dimensions of the analytic and Neural Galerkin solutions are shown in Figure 10.

For the experiment with time and spatially varying coefficients, the initial condition is a sum $u_0(x) = p_1(x)/10 + p_2(x)/10$ of two Gaussian probability density p_1, p_2 functions that are scaled by a factor $1/10$ to avoid scaling issues. The means are

$$\boldsymbol{\mu}_1 = 2 - \frac{1}{12} [-1 \quad 2 \quad -3 \quad 4 \quad -5]^T, \quad \boldsymbol{\mu}_2 = 1.8 - \frac{1}{12} [1 \quad -2 \quad 3 \quad -4 \quad 5]^T$$

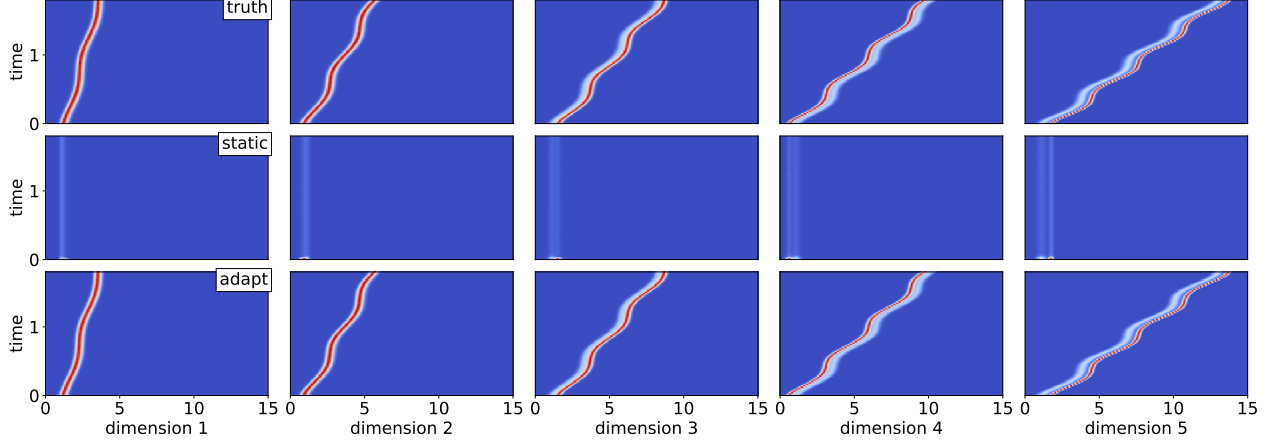


Figure 10.: High-dimensional transport with time-varying coefficient: The plots labeled with “truth” show the marginals of the analytic solution. The plots labeled with “uniform” are the Neural Galerkin approximations with a static uniform sampling in $[0, 15]^d$. The plots labeled with “adapt” show the Neural Galerkin solution with adaptive sampling, which is in close agreement with the analytic solution.

and the covariances are

$$\Sigma_1 = \begin{bmatrix} \frac{3}{50} & & & & \\ & \ddots & & & \\ & & & & \\ & & & & \frac{3}{50} \end{bmatrix}, \quad \Sigma_2 = \begin{bmatrix} \frac{3}{100} & & & & \\ & \ddots & & & \\ & & & & \\ & & & & \frac{3}{100} \end{bmatrix}.$$

The marginals for all five dimensions of the Neural Galerkin solutions are shown in Figure 11. The mean residual is computed as follows: We draw $n = 10^5$ samples from the equally-weighted mixture of Gaussians given by the $m = 50$ nodes of the network at time t . The standard deviation of the Gaussians is double the standard deviation of the nodes of the network. With these samples, we compute a Monte Carlo estimate of the objective J_t at time t .

G. Fokker-Planck equation in high-dimensions

Because the goal is approximating a density, the Neural Galerkin parametrization in this example uses coefficients that are squared to guarantee a non-negative approximation, i.e.,

$$U(\theta, \mathbf{x}) = \sum_{i=1}^m c_i^2 \varphi(\mathbf{x}, w_i, \mathbf{b}_i). \quad (50)$$

The normalized Neural Galerkin approximation is given by

$$\bar{U}(\theta, \mathbf{x}) = \frac{1}{\sum_i c_i^2} \sum_{i=1}^m c_i^2 \varphi(\mathbf{x}, w_i, \mathbf{b}_i). \quad (51)$$

The scaling factor κ in the adaptive sampling is set to $\kappa = 2$ in this experiment.

In case of the harmonic trap, the following system of ODEs describe the mean $\bar{X}_i(t)$ and covariance $C_{ij}(t)$ of particles X_i and X_j at time t for $i, j = 1, \dots, d$ are

$$\dot{\bar{X}}_i(t) = -(1 + \alpha)\bar{X}_i(t) + a(t) + \frac{\alpha}{d} \sum_{j=1}^d \bar{X}_j(t), \quad i = 1, \dots, d, \quad (52)$$

$$\dot{C}_{ij} = -2(1 + \alpha)C_{ij} + \frac{\alpha}{d} \sum_{k=1}^d (C_{kj} + C_{ki}) + 2\beta^{-1}\delta_{ij}, \quad i, j = 1, \dots, d, \quad (53)$$

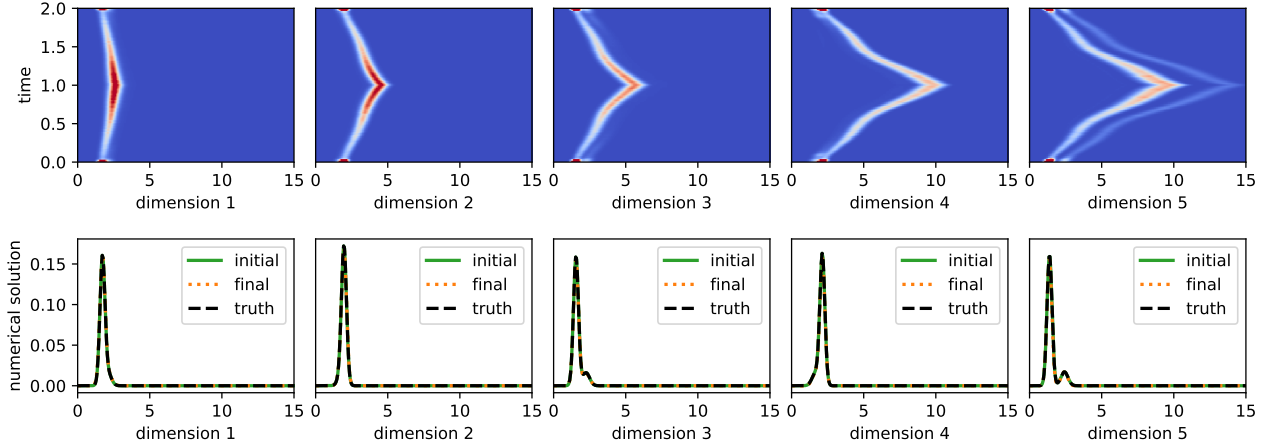


Figure 11.: High-dimensional transport with time and spatially varying coefficients: The first row shows the marginals of the approximation obtained with Neural Galerkin with adaptive sampling and adaptive time integration. Because of the spatially varying coefficient, the coherent structure that is propagated over time changes shape, which is different from the time-only varying case shown in Figure 10. The transport equation is integrated forward and backward in time to compare the approximation at initial and end time, which is shown in the second row. The approximations at initial and end time match well, which indicates that the proposed adaptive approach approximates well the local, high-dimensional dynamics in this problem.

where δ_{ij} is the Dirac delta. The benchmark solution is obtained by integrating these ODEs with Runge-Kutta 45. Figure 12 and 13 compares the particle positions predicted by Neural Galerkin to the benchmark solution for various dimensions.

In case of the aharmonic trap, a Monte Carlo estimate serves as benchmark. To that end, we discretize the stochastic differential equation of the particle positions via the Euler–Maruyama method with time-step size $\delta t = 10^{-4}$ and draw 100,000 paths. From these 100,000 paths we estimate the mean and covariance, which serve as the benchmark for the Neural Galerkin approximation. The particle positions predicted by Neural Galerkin versus the Monte Carlo benchmark are shown in Figure 14.

The entropy of the distribution described by the Neural Galerkin approximation is computed by drawing $n = 5000$ samples $\mathbf{x}_1, \dots, \mathbf{x}_n$ from the mixture given by (50) and then estimating the entropy via Monte Carlo

$$E_n = -\frac{1}{n} \sum_{i=1}^n \log \bar{U}(\theta(t), \mathbf{x}_i).$$

The entropy is approximated via density estimation as follows: We take $n = 5000$ Monte Carlo paths via the Euler–Maruyama method of the stochastic differential equation defining the particle positions. At each time step, we estimate a density with kernel density estimation (KDE) using cross validation over the bandwidth. The estimated density is then used to estimate the entropy via Monte Carlo. In case of the harmonic trap, the entropy can be computed from the covariance estimate given by the ODEs (53) and by exploiting that the solution is Gaussian.

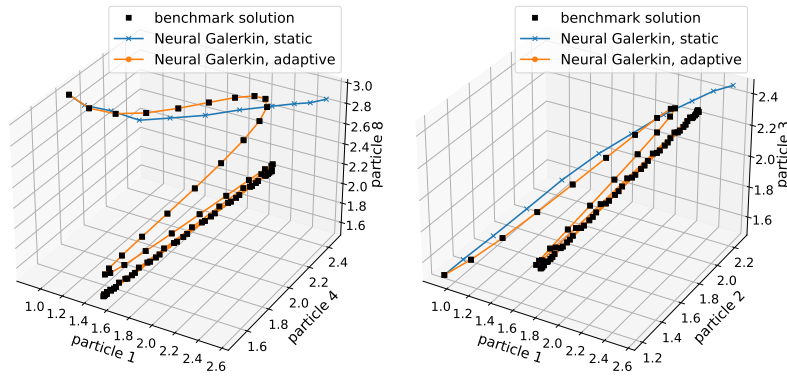


Figure 12.: Particles in harmonic trap: Visualization of particle positions over time.

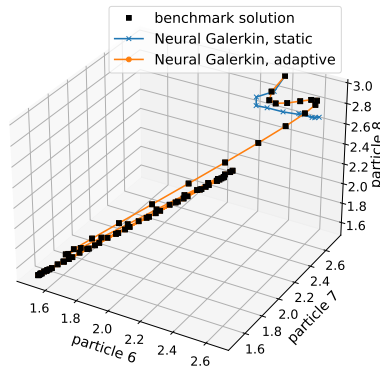


Figure 13.: Particles in harmonic trap: Visualization of particle positions over time.

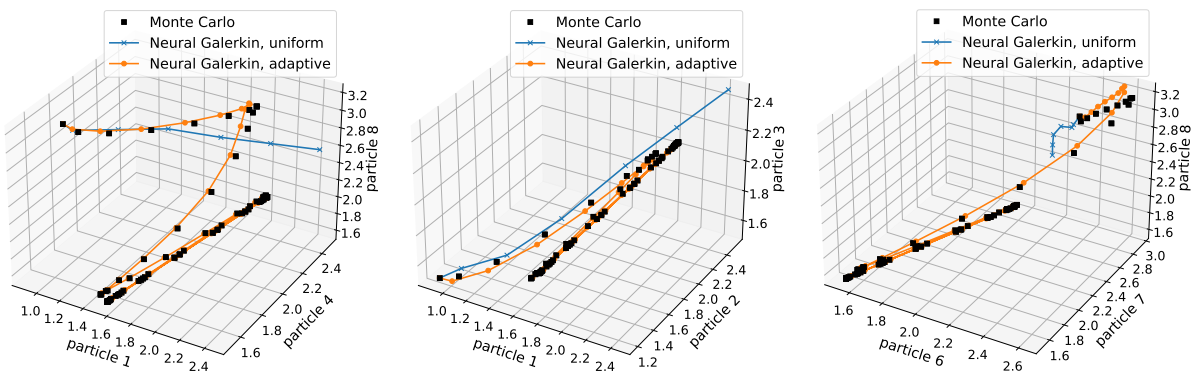


Figure 14.: Particles in anharmonic trap: Visualization of particle positions over time. Note that a Monte Carlo estimate of mean serves as benchmark here.